Kinetic Simulations of the Interruption of Large-Amplitude Shear-Alfvén Waves in a High-β Plasma

J. Squire*
Theoretical Astrophysics, 350-17, California Institute of Technology, Pasadena, California 91125, USA and Walter Burke Institute for Theoretical Physics, California 91125, USA

M. W. Kunz
Department of Astrophysical Sciences, Princeton University, 4 Ivy Lane, Princeton, New Jersey 08544, USA and Princeton Plasma Physics Laboratory, PO Box 451, Princeton, New Jersey 08543, USA

E. Quataert
Astronomy Department and Theoretical Astrophysics Center, University of California, Berkeley, California 94720, USA

A. A. Schekochihin
The Rudolf Peierls Centre for Theoretical Physics, University of Oxford, 1 Keble Road, Oxford OX1 3NP, United Kingdom and Merton College, Oxford OX1 4JD, United Kingdom

(Received 5 May 2017; published 12 October 2017)

Using two-dimensional hybrid-kinetic simulations, we explore the nonlinear "interruption" of standing and traveling shear-Alfvén waves in collisionless plasmas. Interruption involves a self-generated pressure anisotropy removing the restoring force of a linearly polarized Alfvénic perturbation, and occurs for wave amplitudes $\delta B_\perp/B_0 \gtrsim \beta^{-1/2}$ (where β is the ratio of thermal to magnetic pressure). We use highly elongated domains to obtain maximal scale separation between the wave and the ion gyroscale. For standing waves above the amplitude limit, we find that the large-scale magnetic field of the wave decays rapidly. The dynamics are strongly affected by the excitation of oblique firehose modes, which transition into long-lived parallel fluctuations at the ion gyroscale and cause significant particle scattering. Traveling waves are damped more slowly, but are also influenced by small-scale parallel fluctuations created by the decay of firehose modes. Our results demonstrate that collisionless plasmas cannot support linearly polarized Alfvén waves above $\delta B_\perp/B_0 \sim \beta^{-1/2}$. They also provide a vivid illustration of two key aspects of low-collisionality plasma dynamics: (i) the importance of velocity-space instabilities in regulating plasma dynamics at high β, and (ii) how nonlinear collisionless processes can transfer mechanical energy directly from the largest scales into thermal energy and microscale fluctuations, without the need for a scale-by-scale turbulent cascade.

DOI: 10.1103/PhysRevLett.119.155101

Introduction.—Shear-Alfvén (SA) fluctuations are fundamental to magnetized plasma dynamics [1–3]. They are routinely observed in both laboratory and space plasmas [4,5], and are the basis for modern theories of magnetohydrodynamic (MHD) turbulence [6–8]. They are also uniquely robust among plasma waves, with large-scale linear dynamics that are nearly unmodified across both kinetic and fluid plasma models [2].

The purpose of this Letter is to explore, using hybrid-kinetic simulations, an important exception to this robustness. We focus on linearly polarized large-scale SA waves above the "interruption limit" [9,10],

$$\frac{\delta B_\perp}{B_0} \gtrsim \beta^{-1/2}, \tag{1}$$

in a collisionless plasma. Here $\beta \equiv 8\pi p_0/B_0^2$ is the ratio of thermal to magnetic pressure, B_0 is a background magnetic field, and $\delta B_\perp$ is an Alfvénically polarized field perturbation. SA perturbations above the limit (1) rapidly transfer their mechanical energy from the largest scales to plasma microscales and thermal energy, without the help of a turbulent cascade. This paradigm is at odds with standard theories of Alfvénic turbulence in collisionless systems [11], and may be crucial for understanding turbulent energy dissipation in astrophysical plasmas ranging from the intracluster medium (ICM) [12–15] to hot accretion flows [16] and high-β regions of the solar wind [5,17–19].

The interruption of SA perturbations occurs due to the self-generation of pressure anisotropy, $\Delta p \equiv p_\perp - p_\parallel$ (where $p_\perp$ and $p_\parallel$ are the thermal pressures perpendicular and parallel to $\boldsymbol{B}$). Pressure anisotropy is created whenever $B = |\boldsymbol{B}|$ changes in a weakly collisional plasma. If $\beta > 1$, the anisotropic momentum stress $\nabla \cdot (\Delta p \boldsymbol{BB}/B^2)$ can be as important as, or even dominate over, the magnetic tension $\nabla \cdot (\boldsymbol{BB})/4\pi$. This suggests that collisionless dynamics can differ from MHD predictions, even for large-scale

perturbations satisfying $\lambda \gg \rho_i$, $\tau \gg \Omega_i^{-1}$ (where ρ_i and Ω_i are the ion gyroradius and gyrofrequency, respectively).

Interruption occurs when a linearly polarized SA oscillation creates an anisotropy $\Delta p = -B^2/4\pi$, which offsets the magnetic tension and triggers the firehose instability on ion gyroscales [20–23]. Even at small wave amplitudes ($\beta^{-1/2} < \delta B_\perp/B_0 \ll 1$), interruption is a nonlinear effect. We study this behavior using hybrid kinetics (kinetic ions and fluid electrons), in three velocity and two spatial dimensions (the latter is required to capture the two-dimensional oblique firehose instability, which is expected evolve similarly in three spatial dimensions). We consider parallel standing and traveling SA waves in the large-scale-separation limit, $\lambda_{\rm MFP} > \lambda_A \gg \rho_i$ ($\lambda_{\rm MFP}$ and λ_A are the ion mean-free path and SA wavelength), as relevant to many astrophysical systems (e.g., in the ICM $\lambda_{\rm MFP} \sim 10^{11}\rho_i$ [12]). Although the thresholds for the oblique and parallel firehose instabilities differ slightly [23,24], we organize our discussion around the latter ($\Delta p = -B^2/4\pi$) because of its importance for large-scale SA waves.

Hybrid-kinetic method.—By treating electrons as an isothermal massless fluid, the hybrid method removes electron kinetic scales, plasma oscillations, and light waves from the Vlasov-Maxwell equations, reducing simulation cost while retaining kinetic ion dynamics [25,26]. The equations consist of (i) the Vlasov equation for the ion distribution function $f_i(\boldsymbol{x}, \boldsymbol{v}, t)$,

$$\frac{\partial f_i}{\partial t} + \boldsymbol{v}\cdot\frac{\partial f_i}{\partial \boldsymbol{x}} + \frac{q_i}{m_i}\left(\boldsymbol{E} + \frac{1}{c}\boldsymbol{v}\times\boldsymbol{B}\right)\cdot\frac{\partial f_i}{\partial \boldsymbol{v}} = 0, \quad (2)$$

(ii) Faraday's law, $\partial\boldsymbol{B}/\partial t = -c\nabla\times\boldsymbol{E}$, and (iii) a generalized Ohm's law,

$$\boldsymbol{E} + \frac{1}{c}\boldsymbol{u}_i\times\boldsymbol{B} = -\frac{T_e\nabla n_i}{e n_i} + \frac{(\nabla\times\boldsymbol{B})\times\boldsymbol{B}}{4\pi q_i n_i}. \quad (3)$$

Here, q_i and m_i are the ion's charge and mass, $\boldsymbol{E}$ is the electric field, c is the speed of light, and T_e is the electron temperature. The ion density $n_i(\boldsymbol{x}) \equiv \int d\boldsymbol{v}\, f_i$ and bulk velocity $\boldsymbol{u}_i(\boldsymbol{x}) \equiv \int d\boldsymbol{v}\, \boldsymbol{v} f_i$ are calculated from f_i, closing the system.

We use the second-order-accurate particle-in-cell (PIC) code, PEGASUS [27]. We employ the δf method [28], which evolves $\delta f = f - f_0$ rather than f itself, and take f_0 to be an isotropic Maxwellian. This reduces particle noise by $\sim(\delta f/f_0)^2$, making it optimal for simulation of high-β plasmas, where very small ($\ll 1/\beta$) deviations from a Maxwellian distribution must be accurately resolved.

Simulation setup.—We consider two initial conditions, which vary initially only on large scales. These are (i) a parallel standing SA wave initiated by a magnetic perturbation, and (ii) a parallel traveling SA wave. We focus on the standing wave because of its relevance to situations where $\langle dB/dt\rangle \neq 0$, e.g., Alfvénic turbulence ($\langle\cdot\rangle$ represents a spatial average). Although also important, we leave study of initial Alfvénic velocity perturbations to future work, due to the larger domains required to capture mirror instability dynamics [29,30]. The initial ion distribution function is an isotropic Maxwellian with $T_e = T_i$, with a background magnetic field $\boldsymbol{B} = B_0\hat{\boldsymbol{x}}$ and $\beta_i = 8\pi n_i T_i/B_0^2 = 100$. Our domains have width $L_y = 50\rho_i$ and lengths up to $L_x = 1000\rho_i$, to maximize scale separation between the SA wave and microscale dynamics. We use a spatial resolution of $\Delta x = 0.3125\rho_i$ and $N_{\rm PPC} = 4096$ particles per cell (PPC) for the two main simulations in this Letter. We initialize with $\lambda_A = L_x$ in the out-of-plane field, $\delta B_z = -\delta b B_0\cos(2\pi x/\lambda_A)$, and, for the traveling wave, a corresponding velocity perturbation, $\delta u_z = \delta b v_A\cos(2\pi x/\lambda_A)$. In each case, we take the wave amplitude $\delta b = 0.5$, which is well above the interruption limit $\delta b_{\rm max} \approx 2\beta^{-1/2}$ [9]. Within the MHD model, these initial conditions would create continuing sinusoidal SA oscillations of period $\tau_A = 2\pi/\omega_A = \sqrt{\beta_i}\lambda_A/\rho_i\Omega_i^{-1}$ (modified slightly by compressibility [10]).

Because of the wide range of time and space scales involved in this problem, careful numerical tests are crucial. In addition to previous PEGASUS tests [27], we tested the numerical parameters required to accurately propagate long-wavelength linear SA waves (with $\lambda_A/\rho_i =$ 50 to 1000, $\delta b = 0.05$). These tests demonstrated that high $N_{\rm PPC} \propto \lambda_A/\rho_i$ is required for large wavelengths, due to the buildup of PIC noise over long simulation times. For production runs, $N_{\rm PPC} = 4096$ was chosen based on these requirements. We also tested the convergence (with $N_{\rm PPC}$) of nonlinear standing waves at $\lambda_A/\rho_i = 250$, and their dependence on λ_A/ρ_i over the range $\lambda_A/\rho_i = 125$ to 1000. We observed broadly similar dynamics over this range.

Shear-Alfvén standing wave.—Figure 1 shows the spatiotemporal evolution of δB_z for a standing SA wave with $\lambda_A/\rho_i = 1000$, $\tau_A\Omega_i = 10000$ ($\omega_A/\Omega_i = 2\pi\times 10^{-4}$). The pictured snapshots are chosen to illustrate the distinct phases of nonlinear wave evolution. These are (i) initial field decrease, which creates a negative anisotropy $\Delta p < -B^2/4\pi$, nullifying magnetic tension and triggering the firehose instability, (ii) eruption of oblique firehose modes [22,23,31], which push the wave back above $4\pi\Delta p/B^2 = -1$, (iii) decay of oblique firehose modes into smaller-scale ($k_\perp = 0$, $k_\parallel\rho_i \sim 1$) fluctuations that scatter particles and cause the large-scale δB_z to decay, and (iv) dissolution of the wave into freely oscillating SA waves below the limit (1), which can oscillate freely. Of these stages, (iii) is notably different from the predictions of one-dimensional Landau-fluid (LF) models [9,10].

Figure 2 shows one-dimensional (y-averaged) wave profiles. Because of heat fluxes [10], as Δp decreases initially it is nearly homogenous in space [Fig. 2(a)]. This causes oblique firehose modes to erupt suddenly across the entire wave [Fig. 1(b)] at $t/\tau_A \approx 0.075$. These growing

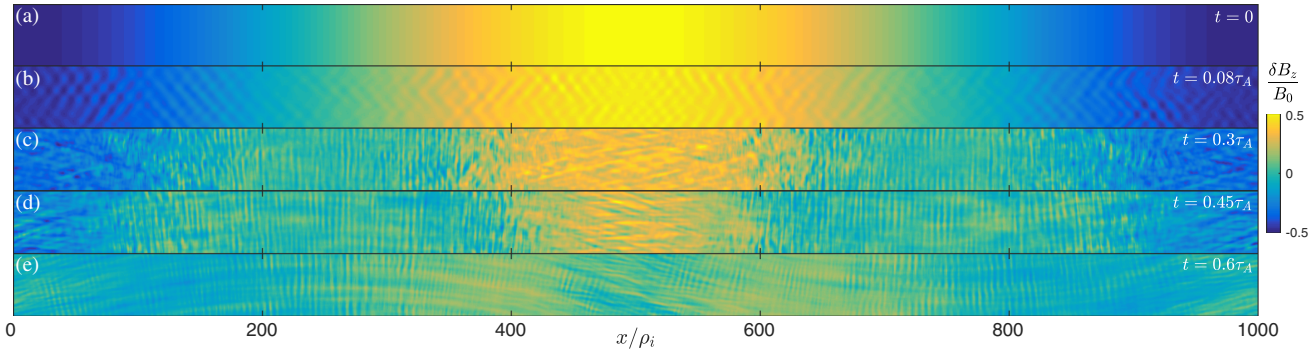

FIG. 1. Out-of-plane magnetic perturbation, $\delta B_z/B_0$, in a standing shear-Alfvén wave at $t = 0$ (a), $t = 0.08\tau_A$ (b), $t = 0.3\tau_A$ (c), $t = 0.45\tau_A$ (d), and $t = 0.6\tau_A$ (e) ($\tau_A = 10^4\Omega_i^{-1}$ is the linear Alfvén period).

modes cause Δp to increase [32] back into the stable regime $\Delta p > -B^2/4\pi$ by $t/\tau_A \approx 0.085$, where it stays until the SA wave decays.

The subsequent evolution of the oblique firehose modes controls the large-scale wave dynamics. If these (now stable) fluctuations scatter particles sufficiently strongly, δB_z can decay with $\Delta p \approx -B^2/4\pi$; if they do not (e.g., if they are resonantly damped [16,29,33]), δB_z cannot decrease [9]. The firehose modes' evolution is governed by Δp [12], which varies in space. Near the wave nodes, where $S = |\nabla \boldsymbol{u}| \approx 0$ and $\delta B_z \approx 0$, Δp is not driven by a large-scale dB/dt and can freely decay [29,32,34,35]. Near the wave antinodes, where $S \sim \beta^{-1/2}\omega_A \approx 6 \times 10^{-5}\Omega_i$ [10] and $\delta B_z \neq 0$, Δp is continuously driven by the decreasing field [29,31,36–38].

Surprisingly, it is small-scale modes at the SA-wave nodes—the least firehose-unstable regions (with $4\pi\Delta p/B^2 \approx -0.7$)—that cause the strongest particle scattering. This is illustrated by the background color in Fig. 2, which shows the effective ion collisionality ν_c/ω_A as a function of space, measured by calculating the time it takes for μ to change by a factor of 1.2 for 2048 sample ions [39]. The scattering changes from being homogenous and weak at early times, to being stronger and localized around the SA-wave nodes at later times. This change is caused by the decay of oblique firehose modes into $k_\parallel \rho_i \sim 1$, $k_\perp \sim 0$ fluctuations [Figs. 1(c) and 1(d)], which scatter particles efficiently due to their small scale. These parallel modes are long lived (they are nonlinearly stabilized against cyclotron damping [40,41]), as indicated by their presence after the large-scale SA wave has decayed and $\Delta p \sim 0$ [Fig. 1(d)].

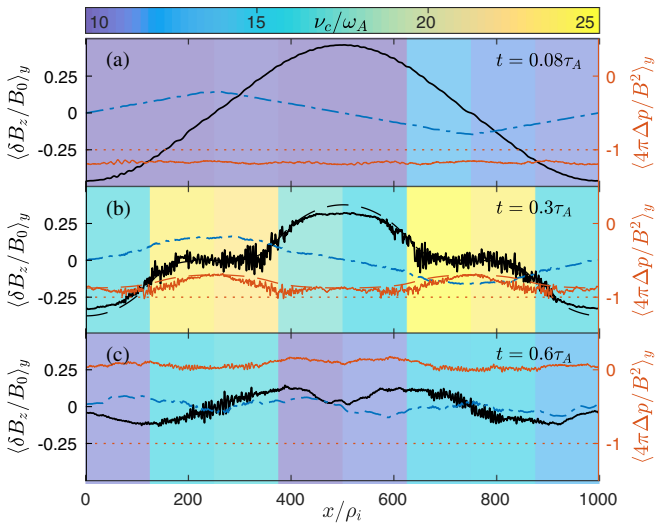

FIG. 2. Evolution of the standing wave from Fig. 1: we show the y-averaged $\delta B_z/B_0$ (black line, left axis), $\delta u_z/v_A$ (blue dot-dashed line, left axis), and firehose parameter $4\pi\Delta p/B^2$ (red, right axis; the dotted red line shows $\Delta p = -B^2/4\pi$), at the times illustrated in Figs. 1(b), 1(c), and 1(e). The background color shows the effective collisionality ν_c/ω_A caused by particle scattering from microscale fluctuations, measured over the time intervals $t/\tau_A \in [0.07, 0.15]$ (a), $t/\tau_A \in [0.2, 0.4]$ (b), and $t/\tau_A \in [0.55, 0.65]$ (c). In (b), we also show (dashed lines) $\delta B_z/B_0$ and $4\pi\Delta p/B^2$ for a decaying SA standing wave in a Braginskii model at $\beta = 100$, $\nu_c/\omega_A \approx 10$ ($\delta u_z/v_A$ is omitted for clarity).

Because $\omega_A \ll \nu_c \ll \Omega_i$, the plasma dynamics now resemble the Braginskii collisional limit [42] and the SA wave behaves as discussed in [10]. We illustrate the similarity in Fig. 2(b), which also shows δB_z and $4\pi\Delta p/B^2$ for an SA wave governed by the Braginskii model (including heat fluxes; see [10], Appendix B). The "humped" shape occurs because the perturbation splits into regions where $4\pi\Delta p \approx -B^2$ and $d\delta B_z/dt < 0$ (around the antinodes), and regions where $4\pi\Delta p > -B^2$ and $\delta B_z = 0$ (these spread from the nodes). The wave decay rate is determined by ν_c, which is sufficiently large [$\nu_c/\omega_A \sim \beta(\delta B_\perp/B_0)^2$] such that the wave decays within $t/\tau_A < 1$. We note parenthetically that the wave decay generates a δB_y perturbation (see Fig. 1), although its origin is currently unclear.

As the large-scale SA wave decays, it heats the plasma. This process does not involve a turbulent cascade, but rather the direct transfer of large-scale mechanical energy into thermal energy. This heating is essentially viscous dissipation, with particle scattering from microscale fluctuations controlling the effective viscosity and making the

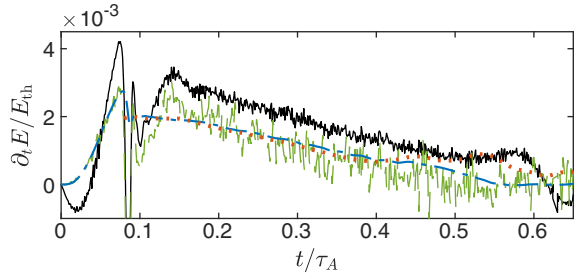

FIG. 3. Plasma heating due to the standing wave in Fig. 1. We compare the rate of change of thermal energy $\partial_t E_{\rm th} = \int d\boldsymbol{x}\, n_i \sum_r \partial_t(\Pi_{rr}/n_i)/2$ (black line; Π_{rs} is the pressure tensor), with mechanical heating $-\int d\boldsymbol{x} \sum_{rs} \Pi_{rs} \nabla_r u_s$ (green dashed line), heating from the large-scale SA wave $\int d\boldsymbol{x}\, \Delta\bar{p}\hat{b}_x\hat{b}_z\partial_x\bar{u}_z$ (blue dot-dashed line; here $\bar{\cdot}$ denotes a filter that smooths fluctuations with $k\rho_i \gtrsim 0.25$), and the approximate viscous heating [43] from the SA wave after interruption $\nu_c^{-1}\int d\boldsymbol{x}\, \bar{p}_\parallel(\hat{b}_x\hat{b}_z\partial_x\bar{u}_z)^2$ (red dotted line; we use $\nu_c/\omega_A \approx 10$ as in Fig. 2). We normalize by $E_{\rm th}$ and use units of τ_A (note the small rates, due to the high β). The initial $\partial_t E_{\rm th} < 0$ is due to the creation of $\boldsymbol{E}$ fluctuations (because of particle noise).

process irreversible. In Fig. 3, we compare the measured $\partial_t E_{\rm th}$ with heating due to the SA wave decay. Although the agreement is not perfect due to spurious grid heating [44] (tests at $\lambda_A/\rho_i = 250$ show that this improves with PPC or reduced λ_A/ρ_i), the stages of wave decay are evident, e.g., the drop in $\partial_t E_{\rm th}$ as firehose fluctuations grow at $t/\tau_A \approx 0.075$, followed by heating as the large-scale $\delta B_\perp$ decays. Figure 3 also shows that the overall energetics are well captured by considering only the large-scale dynamics, or by using the same effective collisionality as in Fig. 2(b). This supports closure models that approximate the effects of microinstabilities on large-scale dynamics without having to resolve the microscales.

Shear-Alfvén traveling wave.—Figures 4 and 5 illustrate the dynamics of the nonlinear SA traveling wave with $\lambda_A = 250\rho_i$. The initial evolution differs from standing waves because $\langle dB/dt\rangle = 0$ for an unperturbed traveling wave, implying that global (spatially constant) pressure anisotropy is created only as the wave decays [9]. The evolution broadly follows the expectations of [9,10], proceeding in four stages: (i) the spatially dependent dB/dt creates an anisotropy $\Delta p(x) \sim \beta^{1/2}\delta B_z^2 \sin(2k_\parallel x)$; (ii) this Δp damps the wave [10,45,46] causing $\langle B\rangle$ to decrease and thus $\langle \Delta p\rangle < 0$; (iii) the wave consequently slows down, with $\delta u_\perp$ decaying faster than $\delta B_\perp$; and (iv) the wave excites oblique firehose modes, which subsequently scatter particles and cause the large-scale $\delta B_\perp$ to decay in a similar manner to the standing wave.

These stages are seen clearly in Figs. 4 and 5. In particular, note the global $\langle \Delta p\rangle < 0$ that quickly develops [Fig. 5(b)] and the fast decay of $\delta u_\perp$ at early times [Fig. 5(c)]. By $t/\tau_A \approx 0.3$, once $\langle \Delta p\rangle$ has decreased sufficiently, the wave starts exciting oblique firehose

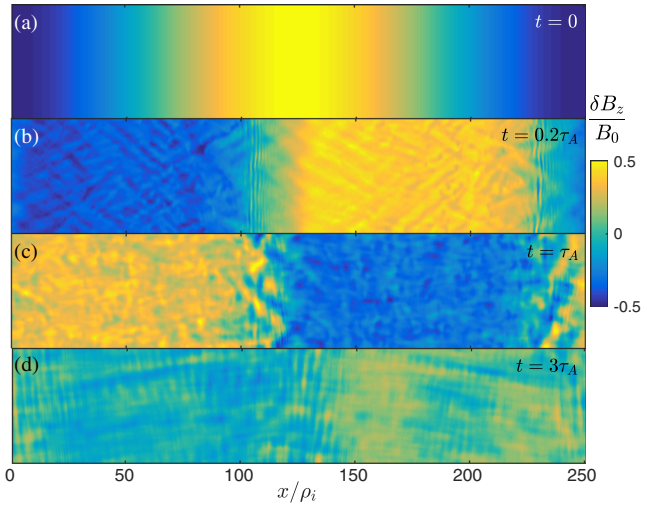

FIG. 4. Out-of-plane magnetic perturbation $\delta B_z/B_0$ for a SA traveling wave with $\lambda_A = 250\rho_i$ at $t = 0$ (a), $t = 0.2\tau_A$ (b), $t = \tau_A$ (c), and $t = 3\tau_A$ (d).

modes. Unlike for standing waves, this occurs only in localized regions around the wave fronts (i.e., near where $\delta B_z = 0$), because $|dB/dt|$ (and thus $|\Delta p|$) is largest in these regions [see, e.g., Fig. 4(c) at $x/\rho_i \approx 110$ and the shading in Fig. 5(b)]. Subsequently, Fig. 5(a) shows that the particle scattering is strongest behind the wavefronts. We

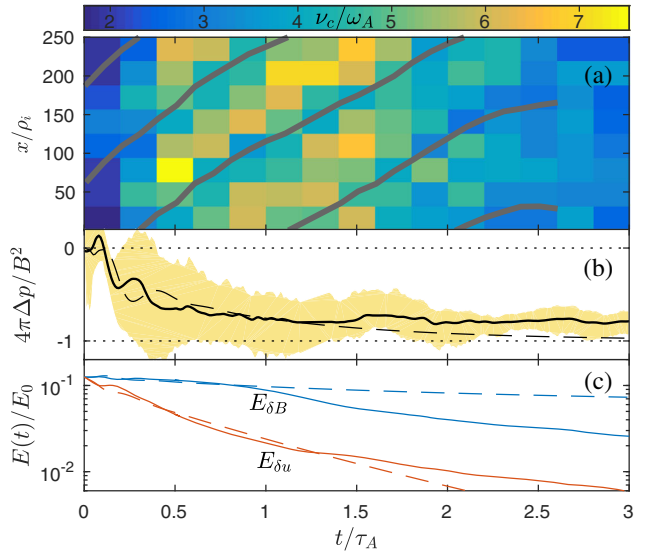

FIG. 5. (a) Scattering rate ν_c/ω_A of the traveling wave in Fig. 4 as a function of x and t. The grey lines follow the wave fronts (this is close to where Δp is most negative). (b) Time evolution of $\langle 4\pi\Delta p/B^2\rangle$. The shaded region indicates the range of $4\pi\Delta p/B^2$ seen across the wave profile, to illustrate when the wave can excite firehose modes. (c) Energy of the magnetic perturbation $E_{\delta B} = \int d\boldsymbol{x}\, \delta B_z^2/8\pi$ (blue) and kinetic energy $E_{\delta u} = \int d\boldsymbol{x}\, \rho\delta u_z^2/2$ (red), normalized by $E_0 = \int d\boldsymbol{x}\, B_0^2/8\pi$. In (b) and (c), we plot the results from an equivalent Landau-fluid simulation [10] (dashed lines), for comparison.

interpret this as being due to the transition of oblique firehose modes into long-lived $k_\parallel \rho_i \sim 1$ fluctuations [see Fig. 4(d)], like in the standing wave. Because firehose modes are excited only briefly around the wavefronts, the scattering rate ν_c/ω_A is lower than for the standing wave. Thus the final decay of the traveling wave's δB_z is slower than the standing wave's, although it is qualitatively similar. At earlier times, the large-scale SA wave evolution matches well the predictions from a one-dimensional LF model at $\beta_i = 100$ [10] (dashed lines in Fig. 5).

Discussion.—We have presented hybrid-kinetic simulations of large-amplitude SA waves in a collisionless plasma. Our results demonstrate clearly the exceptional influence of microinstabilities on the large-scale ($\lambda_A \gg \rho_i$) dynamics of high-β collisionless plasmas, illustrating how the evolution of self-excited oblique firehose modes controls the plasma's fluid properties. The simulations also verify, using a realistic model with kinetic ions, that linearly polarized shear-Alfvénic perturbations do not exist in their linear wave form above the amplitude limit $\delta B_\perp/B_0 \sim \beta^{-1/2}$ [9]. The SA wave dynamics depend strongly on how oblique firehose modes evolve as the plasma becomes stable ($\Delta p \gtrsim -B^2/4\pi$). We find that firehose fluctuations become parallel ($k_\perp = 0$) and move to smaller scales ($k_\parallel \rho_i \sim 1$), surviving nonlinearly throughout the large-scale $\delta B_\perp$ decay and scattering particles at a high rate. These long-lived $k_\parallel \rho_i \sim 1$ modes cause SA standing-wave dynamics in a collisionless plasma to resemble those in a collisional (Braginskii) one [10]. The initial evolution of the traveling wave is effectively collisionless and matches analytic predictions [10]; however, after generating a global negative anisotropy and exciting firehose modes, its final decay resembles the standing wave. For both standing and traveling waves, the simulations provide an interesting example of direct transfer of energy from the largest scales to thermal energy and microscale fluctuations, without a turbulent cascade.

Our simulations cannot fully address what occurs at yet higher λ_A/ρ_i. This will depend on how oblique firehose modes decay and scatter particles, physics that is currently poorly understood. That said, it is clear that SA wave interruption provides a robust mechanism for dissipating energy directly from large-scale perturbations into heat and microinstabilities. Our results suggest that numerical models of weakly collisional high-β plasmas would be better off damping large-amplitude SA waves, rather than letting them freely propagate. One concrete way to achieve this aim might be a LF model with pressure-anisotropy limiters [47] that enhance the collisionality to a rate that is determined by the large-scale Alfvén frequency. More work on developing and validating subgrid models of this kind is underway.

Given the strong deviations from MHD predictions, SA wave interruption could significantly impact the turbulent dynamics of weakly collisional plasmas in a variety of astrophysical environments [43]. Some effects have already been observed in the $\beta \sim 1$ solar wind [17]. Other astrophysical plasmas—for instance the ICM, with $\beta \sim 100$ [12,15]—are likely to be more strongly affected by interruption, and work is underway to assess its impact on turbulence under such conditions.

We thank S. Balbus, S. D. Bale, C. H. K Chen, S. Cowley, B. Dorland, G. Hammett, K. Klein, F. Rincon, L. Sironi, and M. Strumik for useful and enlightening discussions. J. S., A. A. S., and M. W. K. thank the Wolfgang Pauli Institute in Vienna for its hospitality on several occasions. J. S. was funded in part by the Gordon and Betty Moore Foundation through Grant No. GBMF5076 to Lars Bildsten, Eliot Quataert, and E. Sterl Phinney. E. Q. was supported by Simons Investigator awards from the Simons Foundation and NSF Grant No. AST 13-33612. A. A. S. was supported in part by grants from UK STFC and EPSRC. M. W. K. was supported in part by NASA Grant No. NNX16AK09G and U.S. DOE Award No. DE-AC02-09-CH11466.

*jsquire@caltech.edu

[1] H. Alfvén, Nature (London) **150**, 405 (1942).
[2] N. F. Cramer, *The Physics of Alfvén Waves* (John Wiley & Sons, New York, 2011).
[3] G. I. Ogilvie, J. Plasma Phys. **82**, 205820301 (2016).
[4] W. Gekelman, S. Vincena, B. V. Compernolle, G. J. Morales, J. E. Maggs, P. Pribyl, and T. A. Carter, Phys. Plasmas **18**, 055501 (2011).
[5] R. Bruno and V. Carbone, Living Rev. Solar Phys. **10** (2013).
[6] P. Goldreich and S. Sridhar, Astrophys. J. **438**, 763 (1995).
[7] S. Boldyrev, Phys. Rev. Lett. **96**, 115002 (2006).
[8] A. Mallet and A. A. Schekochihin, Mon. Not. R. Astron. Soc. **466**, 3918 (2017).
[9] J. Squire, E. Quataert, and A. A. Schekochihin, Astrophys. J. Lett. **830**, L25 (2016).
[10] J. Squire, A. Schekochihin, and E. Quataert, New J. Phys. **19**, 055005 (2017).
[11] A. A. Schekochihin, S. C. Cowley, W. Dorland, G. W. Hammett, G. G. Howes, E. Quataert, and T. Tatsuno, Astrophys. J. Suppl. Ser. **182**, 310 (2009).
[12] M. S. Rosin, A. A. Schekochihin, F. Rincon, and S. C. Cowley, Mon. Not. R. Astron. Soc. **413**, 7 (2011).
[13] I. Zhuravleva, E. Churazov, A. A. Schekochihin, S. W. Allen, P. Arevalo, A. C. Fabian, W. R. Forman, J. S. Sanders, A. Simionescu, R. Sunyaev, A. Vikhlinin, and N. Werner, Nature (London) **515**, 85 (2014).
[14] J. Peterson and A. Fabian, Phys. Rep. **427**, 1 (2006).
[15] T. A. Enßlin and C. Vogt, Astron. Astrophys. **453**, 447 (2006).
[16] E. Quataert, Astrophys. J. **500**, 978 (1998).
[17] S. D. Bale *et al.* (to be published).
[18] S. D. Bale, J. C. Kasper, G. G. Howes, E. Quataert, C. Salem, and D. Sundkvist, Phys. Rev. Lett. **103**, 211101 (2009).

[19] C. H. K. Chen, J. Plasma Phys. **82**, 535820602 (2016).
[20] R. C. Davidson and H. J. Völk, Phys. Fluids **11**, 2259 (1968).
[21] M. N. Rosenbluth, Technical Report No. LA-2030, 1956, https://www.osti.gov/scitech/biblio/4329910-stability-pinch.
[22] P. H. Yoon, C. S. Wu, and A. S. de Assis, Phys. Fluids B **5**, 1971 (1993).
[23] P. Hellinger and H. Matsumoto, J. Geophys. Res. **105**, 10519 (2000).
[24] K. G. Klein and G. G. Howes, Phys. Plasmas **22**, 032903 (2015).
[25] J. A. Byers, B. I. Cohen, W. C. Condit, and J. D. Hanson, J. Comp. Phys. **27**, 363 (1978).
[26] D. W. Hewett and C. W. Nielson, J. Comp. Phys. **29**, 219 (1978).
[27] M. W. Kunz, J. M. Stone, and X.-N. Bai, J. Comp. Phys. **259**, 154 (2014).
[28] Y. Chen and S. Parker, J. Comp. Phys. **189**, 463 (2003).
[29] S. Melville, A. A. Schekochihin, and M. W. Kunz, Mon. Not. R. Astron. Soc. **459**, 2701 (2016).
[30] F. Rincon, A. A. Schekochihin, and S. C. Cowley, Mon. Not. R. Astron. Soc. **447**, L45 (2015).
[31] M. W. Kunz, A. A. Schekochihin, and J. M. Stone, Phys. Rev. Lett. **112**, 205003 (2014).
[32] A. A. Schekochihin, S. C. Cowley, R. M. Kulsrud, M. S. Rosin, and T. Heinemann, Phys. Rev. Lett. **100**, 081301 (2008).
[33] E. A. Foote and R. M. Kulsrud, Astrophys. J. **233**, 302 (1979).
[34] K. B. Quest and V. D. Shapiro, J. Geophys. Res. **101**, 24457 (1996).
[35] J. Seough, P. H. Yoon, and J. Hwang, Phys. Plasmas **22**, 012303 (2015).
[36] L. Matteini, S. Landi, P. Hellinger, and M. Velli, J. Geophys. Res. **111**, A10101 (2006).
[37] P. Hellinger and P. M. Trávníček, J. Geophys. Res. **113**, A10109 (2008).
[38] M. A. Riquelme, E. Quataert, and D. Verscharen, Astrophys. J. **824**, 123 (2016).
[39] We then rescale ν_c so that ν_c^{-1} measures factor-e changes in μ.
[40] S. P. Gary and S. Saito, J. Geophys. Res. **108**, 373 (2003).
[41] S. P. Gary, J. Geophys. Res. **109**, 1483 (2004).
[42] S. I. Braginskii, Rev. Plasma Phys. **1**, 205 (1965).
[43] M. W. Kunz, A. A. Schekochihin, S. C. Cowley, J. J. Binney, and J. S. Sanders, Mon. Not. R. Astron. Soc. **410**, 2446 (2011).
[44] C. K. Birdsall and A. B. Langdon, *Plasma Physics via Computer Simulation* (Adam Hilger, Bristol, England, 1991).
[45] M. A. Lee and H. J. Völk, Astrophys. Space Sci. **24**, 31 (1973).
[46] R. M. Kulsrud, in *Astronomical Papers Dedicated to Bengt Stromgren*, edited by A. Reiz and T. Andersen (1978), pp. 317–326.
[47] P. Sharma, G. W. Hammett, E. Quataert, and J. M. Stone, Astrophys. J. Lett. **637**, 952 (2006).